

AD-A246 776



Technical Report  
934

## Scattering Measurements and Predictions for a Delta Stage II Rocket Nozzle

DTIC  
ELECTE  
MAR 4 1992  
S B D

T.G. Moore

3 January 1992

**Lincoln Laboratory**

MASSACHUSETTS INSTITUTE OF TECHNOLOGY

LEXINGTON, MASSACHUSETTS



Prepared for the Department of the Air Force  
under Contract F19628-90-C-0002.

Approved for public release; distribution is unlimited.

92-04992



92 2 26 011

This report is based on studies performed at Lincoln Laboratory, a center for research operated by Massachusetts Institute of Technology. The work was sponsored by the Department of the Air Force under Contract F19628-90-C-0002.

This report may be reproduced to satisfy needs of U.S. Government agencies.

The ESD Public Affairs Office has reviewed this report, and it is releasable to the National Technical Information Service, where it will be available to the general public, including foreign nationals.

This technical report has been reviewed and is approved for publication.

FOR THE COMMANDER

*Hugh L. Southall*

Hugh L. Southall, Lt. Col., USAF  
Chief, ESD Lincoln Laboratory Project Office

Non-Lincoln Recipients

PLEASE DO NOT RETURN

Permission is given to destroy this document  
when it is no longer needed.

MASSACHUSETTS INSTITUTE OF TECHNOLOGY  
LINCOLN LABORATORY

**SCATTERING MEASUREMENTS AND PREDICTIONS FOR A  
DELTA STAGE II ROCKET NOZZLE**

*T.G. MOORE*  
*Group 93*

TECHNICAL REPORT 934

3 JANUARY 1992

Approved for public release; distribution is unlimited.

LEXINGTON

MASSACHUSETTS

## ABSTRACT

This report develops the theory necessary to analyze radar images of non-conical rocket nozzle sections. The theory is based on Geometric Optics and ray tracing. The location of the expected response in an inverse synthetic-aperture radar image of this type of rocket nozzle is developed. The ability to predict the location of the response is used to develop a technique for reconstructing the shape of a rocket nozzle from measurements made from an image.

The theory is applied to a pass of data collected on a tumbling Delta Stage II rocket body. The data were collected by a millimeter-wave radar with a center frequency of 35 GHz and a bandwidth of 1 GHz. The theoretical predictions of the scattered fields are first validated using these data and drawings of the rocket nozzle. The inverse method is then applied to the data to determine the shape of the nozzle. The agreement between the nozzle shape predicted by the inverse method and drawings of the nozzle agree to within 6 percent.



<b>Accession For</b>	
NTIS GRA&I	<input checked="" type="checkbox"/>
DTIC TAB	<input type="checkbox"/>
Unannounced	<input type="checkbox"/>
Justification	
By	
Distribution/	
Availability Codes	
Dist	Avail and/or Special
A-1	

## TABLE OF CONTENTS

Abstract	iii
List of Illustrations	vii
1. INTRODUCTION	1
2. THEORY	3
2.1 One-Bounce Ray	6
2.2 Two-Bounce Ray	6
2.3 Three-Bounce Ray	8
3. DELTA STAGE II ROCKET NOZZLE	13
4. INVERSE PROBLEM	19
5. SUMMARY	23
APPENDIX A - SURFACE PARAMETERS FOR A BODY OF REVOLUTION	25
APPENDIX B - SURFACE PARAMETERS FOR THE NOZZLE	29
REFERENCES	31

## LIST OF ILLUSTRATIONS

Figure No.		Page
1	Rocket-nozzle scattering geometry.	4
2	Scattering geometry for a single-reflection specular.	7
3	Scattering geometry for a two-reflection specular.	9
4	Scattering geometry for a three-reflection specular.	10
5	Rocket-nozzle scattering geometry.	12
6	Comparison between the fitted ellipse and the digitized points.	14
7	Comparison between the measured extended return length and the uncorrected calculated return length. The dots are the measurements with one-half resolution-cell error bars.	15
8	Calculated corrections to the extended return length due to nonuniform Doppler shifts.	15
9	Comparison between the measured extended return length and the corrected calculated return length. The dots are the measurements with one-half resolution-cell error bars.	16
10	Reflection locations. The upper curve defines the location of the first reflection and the lower curve defines the location of the second reflection.	17
11	Comparison of the predicted (dashed) and measured radar cross section of the multiple reflection.	18
12	Image-measurement coordinate system.	20
13	Depiction of the optimization loop.	21
A-1	Body-of-revolution coordinate system.	27

## 1. INTRODUCTION

The interaction between electromagnetic waves and cavities often exhibits very distinguishable scattering patterns. One method for extracting information from the scattered field is to form a radar image [1]. This technique is very useful if the frequency of the incident field is not near a resonance of the cavity. One of the distinguishing features in an image of a cavity is a return that is visible downrange from the entrance of the cavity. This extended return is the result of energy trapped inside the cavity that later exits toward the radar. By measuring the characteristics of this extended return it may be possible to determine information about the cavity.

In order to study the phenomenology of scattering from cavities, this report examines a common geometry—a rocket nozzle. Rocket nozzles are commonly found on tumbling rocket bodies that are left in an earth orbit. At times it is useful to try to determine the condition, or shape/size, of a rocket nozzle on a tumbling rocket body. To derive such information, an understanding must be developed of how radar energy scatters from such nozzles. This report will examine the scattering from a non-conic rocket nozzle and address the question of estimating the shape of the nozzle from measurements made from radar images.

The remainder of this report is as follows. Section 2 develops the theory to predict the scattered field from the interior of the rocket nozzle, using Geometric Optics [2]. Section 3 applies the theory developed in Section 2 to a known rocket nozzle. The predicted location and intensity of the scattered field are compared with those measured from a radar image. Section 4 develops the framework necessary to extract the parameters of a rocket nozzle based on measurements from radar images. This technique is applied to the rocket nozzle data that were used in Section 3. Section 5 summarizes the developments of the previous sections.

## 2. THEORY

In this section Geometric Optics (GO) [2] is used to compute the electromagnetic scattering from a rocket nozzle. For this method to be valid, the nozzle is assumed to be large compared to the incident field's wavelength and the frequency of the incident field is assumed to be far from a resonance point of the nozzle cavity. The problem is made tractable by assuming that the rocket nozzle is a body of revolution and that the generating arc can be approximated by a section of an ellipse. Under these assumptions the surface of the nozzle is described as

$$\mathbf{r}(\psi, \phi) = A \cos(\psi) \hat{\mathbf{z}} + B \sin(\psi) (\hat{\mathbf{x}} \cos \phi + \hat{\mathbf{y}} \sin \phi) + \mathbf{r}_0 \quad , \quad (1)$$

where the parameters  $\psi$  and  $\phi$  are defined by

$$\psi_0 \leq \psi \leq \psi_1, \quad 0 \leq \phi \leq 2\pi \quad (2)$$

and the unit vectors  $\hat{\mathbf{x}}$ ,  $\hat{\mathbf{y}}$ , and  $\hat{\mathbf{z}}$  are defined in Figure 1. The parameters  $A$  and  $B$  describe the elliptical generating arc of the body. The inward normal to the surface is found to be

$$\mathbf{n}(\psi, \phi) = -B \cos(\psi) \hat{\mathbf{z}} - A \sin(\psi) (\hat{\mathbf{x}} \cos \phi + \hat{\mathbf{y}} \sin \phi) \quad . \quad (3)$$

The nozzle is illuminated by a sinusoidal plane wave with the normal to the phase front depressed by an angle  $\theta$  from the body symmetry axis. Therefore, the incident field at any point in space is described by

$$\mathbf{E}^i = \mathbf{e}^i e^{-jk\hat{\mathbf{s}} \cdot \mathbf{r} - j\omega t} \quad , \quad (4)$$

where  $\mathbf{r}$  is a position vector in space,  $\mathbf{e}^i$  is the polarization vector, and the direction vector  $\hat{\mathbf{s}}$  is given by

$$\hat{\mathbf{s}} = \cos(\theta) \hat{\mathbf{z}} + \sin(\theta) \hat{\mathbf{x}} \quad . \quad (5)$$

Without loss of generality, the direction vector of the incident field is restricted to lie in the  $X - Z$  plane.

To compute the scattering of the incident field inside of the rocket nozzle, Geometric Optics is employed. This involves decomposing the incident field into an infinite number of ray tubes, then tracing the ray tubes as they reflect within the nozzle. This procedure begins by tracking an unshadowed ray that enters the cavity as the ray intercepts the upper surface ( $\psi > 0$ ) of the

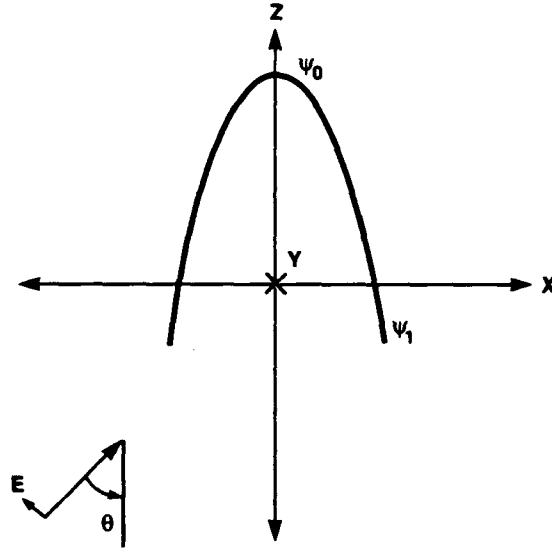


Figure 1. Rocket-nozzle scattering geometry.

nozzle at some point  $\psi^i$  and reflects from this surface according to Snell's law. According to GO and Snell's law, the reflected ray can be described by

$$\mathbf{E}^r = \mathbf{E}^i(\psi^i, \phi^i) \cdot \bar{\mathbf{R}} A(\psi^i, s) e^{-jks} \quad , \quad (6)$$

where  $A(\psi^i, s)$  is the wavefront divergence factor and  $\bar{\mathbf{R}}$  is the dyadic reflection coefficient. The parameters  $\psi^i$  and  $\phi^i$  indicate the point on the surface where the ray is reflecting from. The wavefront divergence factor is given by

$$A(\psi, s) = \sqrt{\frac{\rho_1^r \rho_2^r}{(\rho_1^r + s)(\rho_2^r + s)}} \quad , \quad (7)$$

where  $\rho_1^r$  and  $\rho_2^r$  are the reflected wavefront curvatures. See Balanis [3] for a complete discussion on the computation of the wavefront curvatures. The wavefront divergence factor is simplified by assuming that  $s$  is large compared to the radii of curvature. Under these assumptions  $A$  reduces to

$$A(s; \psi) \sim \frac{\sqrt{\rho_1^r \rho_2^r}}{s} \quad . \quad (8)$$

where

$$\rho_1^r \rho_2^r = R_1 R_2 / 4 \quad (9)$$

However, the full form for  $A(s; \psi)$  is needed for the interior reflections. The right-hand side of the above equation is the product of the principle radii of curvatures of the surface the incident wave is reflecting from. The expression for the product of the curvatures, derived in Appendix B, follows:

$$\frac{R_1 R_2}{4} = \frac{(A^2 \sin^2 \psi + B^2 \cos^2 \psi)^2}{4AB} \quad (10)$$

The asymptotic form of  $A$ , (8), will be referred to as  $A(\psi)$ , where we have suppressed the  $\frac{1}{s}$ .

The dyadic reflection coefficient  $\bar{\mathbf{R}}$  is given by

$$\bar{\mathbf{R}} = \mathbf{e}_{\parallel}^i \mathbf{e}_{\parallel}^r - \mathbf{e}_{\perp}^i \mathbf{e}_{\perp}^r \quad (11)$$

where the unit polarization vectors in the local coordinate system are given by

$$\mathbf{e}_{\perp}^i = \mathbf{e}_{\perp}^r = \hat{\mathbf{y}} \quad (12)$$

and

$$\hat{\mathbf{s}}^i \times \mathbf{e}_{\perp}^i = \mathbf{e}_{\parallel}^i \quad (13)$$

$$\hat{\mathbf{s}}^r \times \mathbf{e}_{\perp}^r = \mathbf{e}_{\parallel}^r \quad (14)$$

From (6), the radar cross section can be determined through the following relationship:

$$\sigma = 4\pi |\mathbf{E}^r \cdot \mathbf{e}^r|^2 \quad (15)$$

where  $\mathbf{e}^r$  is defined as the receive polarization.

Once the scattered field has been determined, it is straightforward to calculate the location of the response in an image. The total path length the ray travels, with the path length from the radar to the origin of the coordinate system removed, will locate the point in range. The location of the response in cross-range is determined by the Doppler shift of the scattered field. The Doppler shift is computed by calculating the rate of change of the scattered fields phase (range) with respect to

the aspect angle change. This mapping of the scattered field on to the range, range-rate coordinate system forms the radar image. In the remainder of this report, the range to the response function,  $R$ , will always have  $r_0 = 0$ .

## 2.1 One-Bounce Ray

A direct specular return will occur when a ray reflects off the top surface and returns toward the radar (see Figure 2). From the above theory, this ray can be written as

$$\mathbf{E}^r = [\mathbf{E}^i(\psi^i, \phi^i) \cdot \bar{\mathbf{R}}(\psi^i, \phi^i)] A(\psi^i, \phi^i) e^{jks} \quad . \quad (16)$$

The specular location will occur when

$$\hat{\mathbf{s}}^i \cdot \hat{\mathbf{n}}(\psi^i, \phi^i) = -1 \quad . \quad (17)$$

This implies that  $\phi^i = 0$  and

$$\tan \psi^i = \frac{B}{A} \tan \theta \quad . \quad (18)$$

In practice, this ray does not occur because it is shadowed by the lower surface.

## 2.2 Two-Bounce Ray

This section examines a ray which reflects twice before it returns toward the radar. This ray will show up in an image made with orthogonal polarized data. The ray that meets this criteria can be shown to reflect only off the upper surface; this ray is depicted in Figure 3. Based on the theory developed previously, the reflected ray can be written as

$$\mathbf{E}^{rr} = [\mathbf{E}^i(\psi^i, \phi^i) \cdot \bar{\mathbf{R}}(\psi^i, \phi^i) \cdot \bar{\mathbf{R}}(\psi^i, \phi^r)] A(\psi^i, \phi^i) A(s; \psi^i, \phi^i) e^{jk(s+\delta r)} \quad . \quad (19)$$

Due to the geometry of this ray,  $\psi^i = \psi^r$ . It is necessary to determine the locations on the surface,  $\psi, \phi$  where the ray reflects from.

The most efficient manner for finding the reflection locations is to track the normal of the wavefront as it reflects off the various surfaces of the nozzle. This is accomplished by using Snell's law to determine the reflected ray's direction. For a ray that reflects off a metal surface, the reflected ray's direction is written as

$$\hat{\mathbf{s}}^r = \hat{\mathbf{s}} - 2 (\hat{\mathbf{s}} \cdot \hat{\mathbf{n}}(\psi^i, \phi^i)) \hat{\mathbf{n}}(\psi^i, \phi^i) \quad . \quad (20)$$

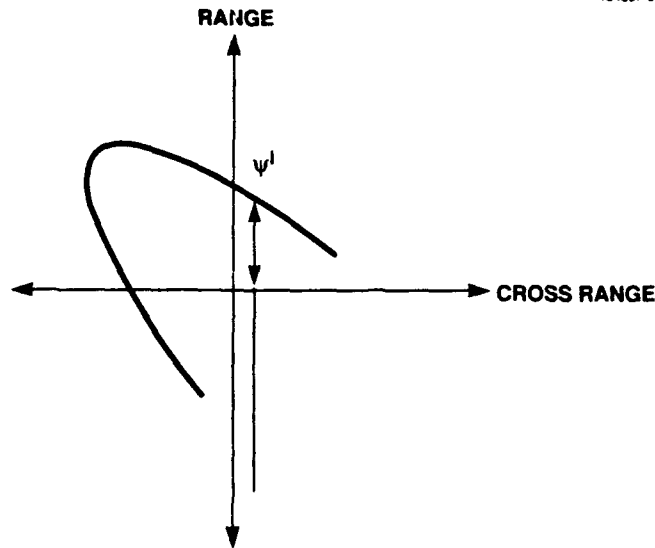


Figure 2. Scattering geometry for a single-reflection specular.

where  $\hat{n}$  is the unit vector in the direction of  $n(\psi, \phi)$ , as defined by (3).

Using this technique, an incident ray  $\hat{s}^i$  is traced as it reflects off one surface and forms a new ray  $\hat{s}^r$ . This ray will then hit the upper surface of the nozzle at a different  $\phi$  location and reflect toward the radar, forming the ray  $\hat{s}^{rr}$ . Due to the symmetry of this problem, a number of constraints can be put on the path of this ray. In order for the ray to return to the radar after two reflections, the reflected ray must meet the following two conditions:

$$\mathbf{s}^r \cdot \mathbf{s}^i = 0 \quad (21)$$

and

$$0 \leq \phi \leq \pi \quad (22)$$

The above expressions lead to analytical expressions for the location of the reflection point:

$$\cos \phi^i = \pm \frac{\tan \theta}{\sqrt{1 + 2 \tan^2 \theta}} \quad (23)$$

and

$$\tan \psi^i = \pm \frac{B}{A} \sqrt{1 + 2 \tan^2 \theta} \quad (24)$$

In practice, this ray is shadowed by the lower surface for most aspect angles.

The extended return range delay is given by  $\delta r = | \tilde{r}(\psi^i, \phi^i) - \tilde{r}(\psi^r, \phi^r) |$ . The apparent range of the response for a given  $\psi$  location will be

$$R(\theta) = \hat{s} \cdot \tilde{r}(\psi^i, \phi^i) + \delta r \quad , \quad (25)$$

which, after substituting in the results obtained earlier, becomes

$$R(\theta) = A \cos \theta \cos \psi^i + B \sin \theta \sin \psi^i \cos \phi^i + 2(B \sin \phi^i \sin \psi^i) \quad (26)$$

In a radar image the response will appear in cross range at

$$X_{pos} = \frac{dR(\theta)}{d\theta} \quad , \quad (27)$$

which, after the appropriate substitutions, becomes

$$\begin{aligned} X_{pos} = & \left( -A \sin \theta \cos \psi^i + B \cos \theta \sin \psi^i \right) \\ & + \left( -A \cos \theta \sin \psi^i + B \sin \theta \cos \psi^i \right) \frac{d\psi^i}{d\theta} \\ & + 2(B \cos \phi^i \sin \psi^i) \frac{d\phi^i}{d\theta} \\ & + 2(B \sin \phi^i \cos \psi^i) \frac{d\psi^i}{d\theta} \quad . \end{aligned} \quad (28)$$

### 2.3 Three-Bounce Ray

This section considers a ray that reflects three times before it exits the nozzle and returns toward the radar. This ray will appear as an extended return in a radar image made with principal polarized data. This ray can be shown to take a path that reflects off one surface of the nozzle and then off the bottom surface directly toward the same point on the upper surface from which it

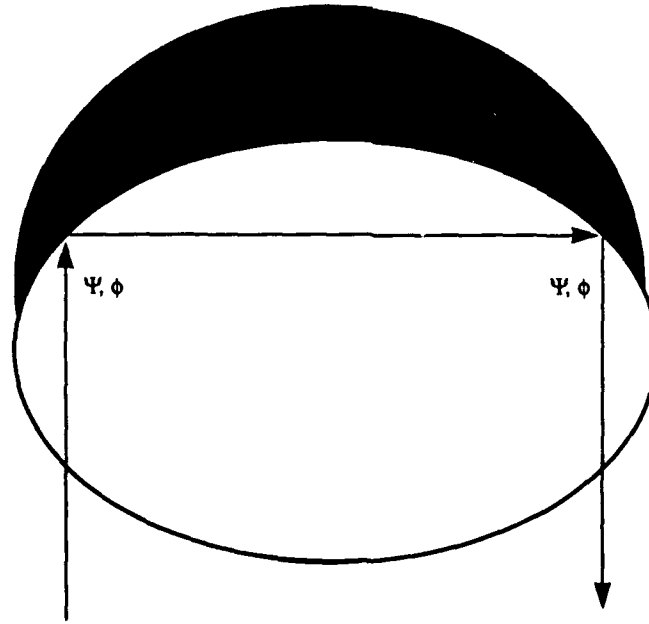


Figure 9. Scattering geometry for a two-reflection specular.

originated. This process is depicted in Figure 4. Based on this theory, the form of this ray can be written as

$$\mathbf{E}^{rrr} = \left[ \mathbf{E}^i(\psi^i) \cdot \bar{\mathbf{R}}(\psi^i) \cdot \bar{\mathbf{R}}(\psi^r) \cdot \bar{\mathbf{R}}(\psi^i) \right] A(\psi^i) A(\delta r; \psi^r) A(\delta r; \psi^i) e^{jk(s+2\delta r)} \quad , \quad (29)$$

where  $\delta r$  is the additional path the ray traverses before returning to the radar. The parameters  $\psi^i$  and  $\psi^r$  represent the points on the surface of the nozzle.

It is necessary to determine the two locations  $\psi^i$  and  $\psi^r$ . The method from the previous section is used to track the normal to the wavefront. Using this technique, an incident ray  $\hat{s}^i$  is tracked as it reflects off one surface and forms a new ray  $\hat{s}^r$ . This ray will then hit the bottom surface of the nozzle and reflect again, forming the ray  $\hat{s}^{rr}$ . For the three-reflection ray to exist, there must be one ray that will reflect from the bottom surface back along its own ray path. This ray occurs when the surface normal at the lower reflection point is parallel to the incoming ray. It is analytically very difficult to determine *a priori* which ray will meet this criteria.

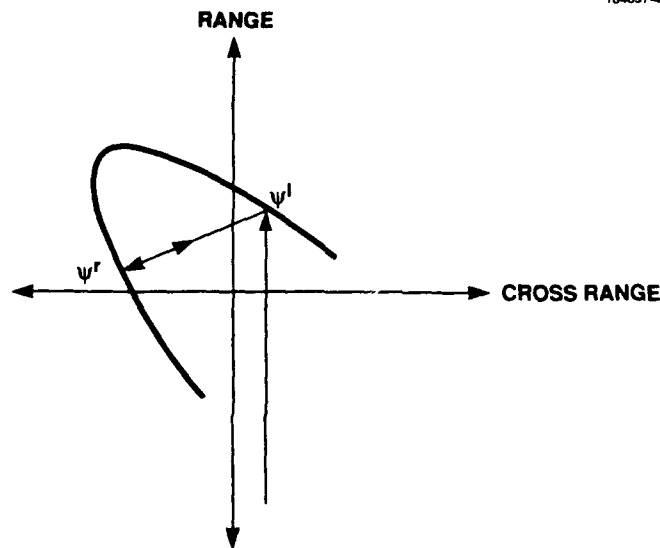


Figure 4. Scattering geometry for a three-reflection specular.

A numerical search scheme is used to find the ray that meets this criteria. The numerical scheme for the three-reflection ray is based on minimizing the function

$$\mathcal{F}(\psi^i; \theta) = \left( -1 - \hat{s}^r(\psi^i) \cdot \hat{n}(\psi^r(\psi^i)) \right)^2, \quad (30)$$

where  $\psi^r(\psi^i)$  is the point at which a ray intercepting the upper surface at  $\psi^i$  would intercept the lower surface. The function  $\mathcal{F}$  will be zero, a minimum, at the correct point. The numerical minimization is implemented in a Mathematica<sup>1</sup> program.

The extended return length for this case is given by  $\delta r = | \vec{r}(\psi^i) - \vec{r}(\psi^r) |$ . The apparent range of the response will be

$$R(\theta) = \hat{s} \cdot \vec{r}(\psi^i) + \delta r, \quad (31)$$

which, after substituting in the results obtained earlier, becomes

<sup>1</sup>Mathematica is a registered trademark of Wolfram Research.

$$R(\theta) = A \cos \theta \cos \psi^i + B \sin \theta \sin \psi^i + \delta r \quad . \quad (32)$$

The response will show up in cross range in the radar image at

$$X_{pos} = \frac{dR(\theta)}{d\theta} \quad . \quad (33)$$

Upon performing the differentiation,

$$\begin{aligned} X_{pos} = & \left( -A \sin \theta \cos \psi^i + B \cos \theta \sin \psi^i \right) \\ & + \left( -A \cos \theta \sin \psi^i + B \sin \theta \cos \psi^i \right) \frac{d\psi^i}{d\theta} \\ & + \frac{d\delta r}{d\theta} \end{aligned} \quad (34)$$

is obtained for the cross-range position of the response. This process is depicted in Figure 5. The first term in the expression corresponds to the true cross-range position of the reflection point. The additional shift in cross range of the extended return is due to the dependence of the extended return on aspect angle. The additional shift can be written as

$$X_{err} = \left( -A \cos \theta \sin \psi^i + B \sin \theta \cos \psi^i \right) \frac{d\psi^i}{d\theta} + \frac{d\delta r}{d\theta} \quad , \quad (35)$$

where this term is denoted as an error term. The additional shift in cross range can lead to errors in measuring the extended return distances from radar images.

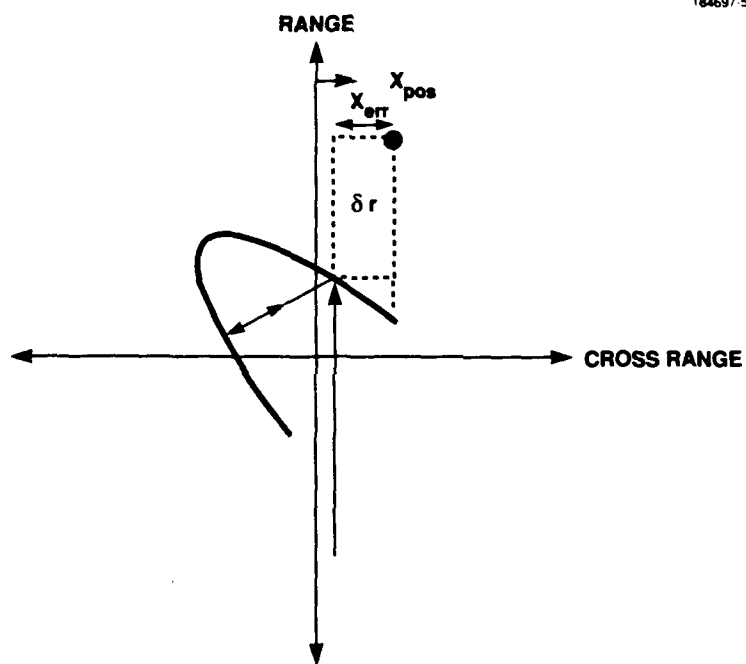


Figure 5. Rocket-nozzle scattering geometry.

### 3. DELTA STAGE II ROCKET NOZZLE

In this section the theory developed in Section 2 is applied to the case of a Delta II Second Stage rocket nozzle. Data were obtained from images produced at the Millimeter-Wave Radar located on the Kwajalein Atoll in the Marshall Islands. The images were made at a center frequency of 35 GHz, with a bandwidth of 1 GHz and an integration angle of approximately 1.4 degrees. This leads to equal range and cross-range resolutions of 28 cm.

As the configuration of the rocket nozzle is known, measurements of the extended return distances were obtained directly from the images. These measurements were made by determining the correct motion solution for the tumbling rocket body, then overlaying a wire-frame model. The distance in range from the response to the wireframe of the nozzle surface was measured. The model was derived from plans of the rocket body, so it can assumed to be exact to within a measurement error less than that of the radar image.

In order to make predictions of the extended returns it was necessary to determine the parameters  $A$  and  $B$  for the generating arc. These parameters were estimated by fitting an ellipse to a digitized representation of the nozzle. The following parameters were determined to be the best fit:

$$\begin{aligned} A &= 8.04 \text{ m}, \\ B &= 1.21 \text{ m}, \\ \psi_0 &= 12 \text{ deg}, \\ \psi_1 &= 42 \text{ deg}. \end{aligned} \tag{36}$$

Figure 6 shows the relationship between the fitted ellipse and the data points. Using these parameters, predictions of the extended return distance were calculated for a sequence of images. Figure 7 shows a comparison between the measured and predicted extended returns and demonstrates a slight discrepancy between the measured and predicted responses. As mentioned in Section 2, there is an additional Doppler offset in the extended return response. This leads to an error in measuring the extended return from the images. Figure 8 shows the magnitude of this error. Figure 9 shows a comparison between the calculated and measured data after the measurement error has been corrected. Although the correction is small, it is enough to make a difference in the minimization loop. These figures demonstrate that by correcting for the Doppler shift it is possible to reduce the error between the predictions and the measurements. In general, the Doppler shift is less than a resolution cell; thus, this bias error can be ignored for most problems. Figure 10 shows the location on the ellipse of the two reflection locations. The upper curve is the first reflection location, the lower curve the second. Figure 11 compares the predicted RCS to the measured RCS for the range of angles considered in this section. In order to obtain the level of agreement demonstrated

in Figure 11, it is necessary to assume that the interior of the nozzle has a reflection coefficient of  $\rho = 0.74$ .

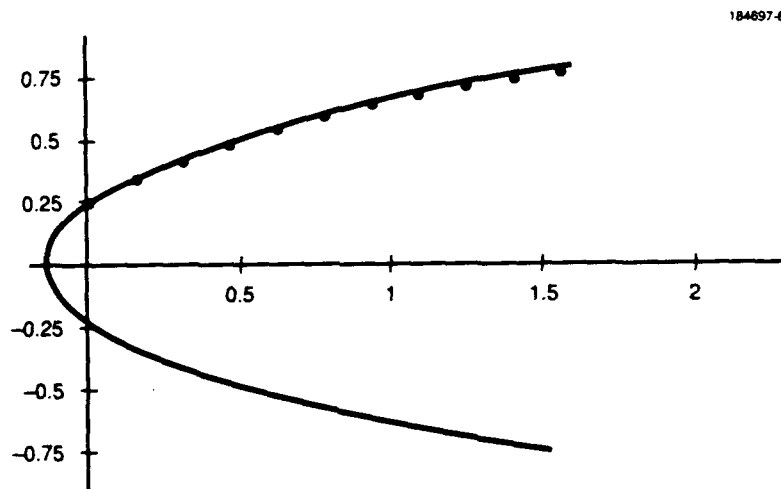


Figure 6. Comparison between the fitted ellipse and the digitized points.

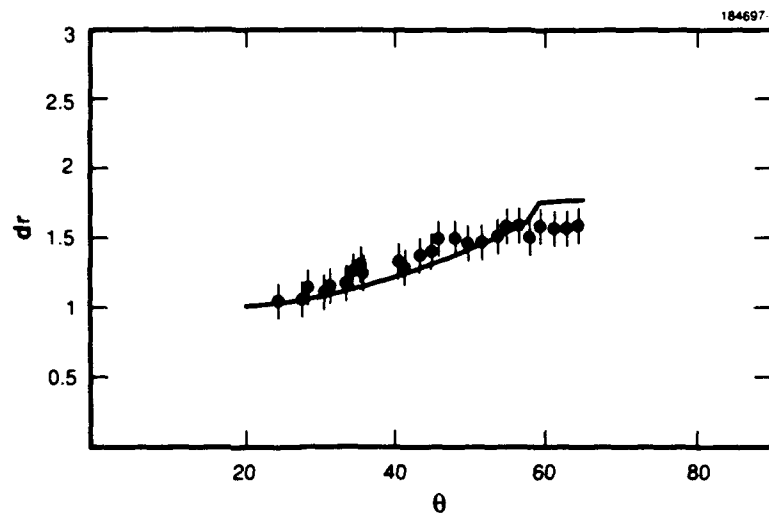


Figure 7. Comparison between the measured extended return length and the uncorrected calculated return length. The dots are the measurements with one-half resolution-cell error bars.

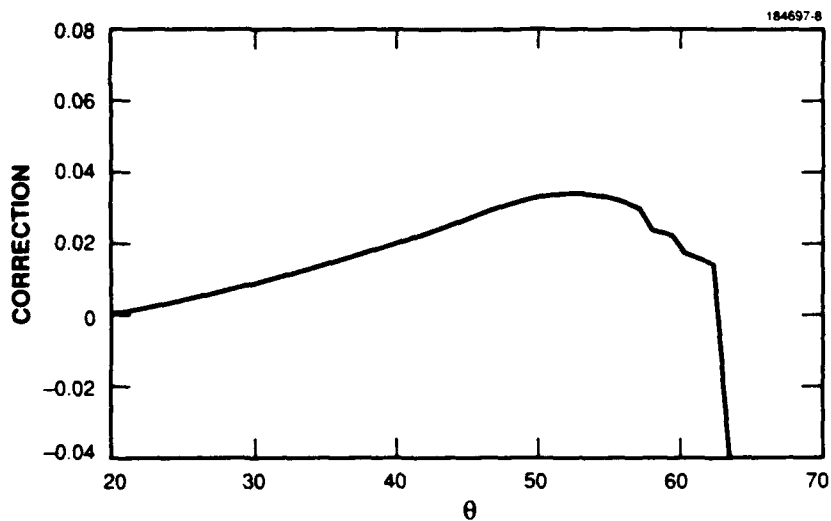


Figure 8. Calculated corrections to the extended return length due to nonuniform Doppler shifts.

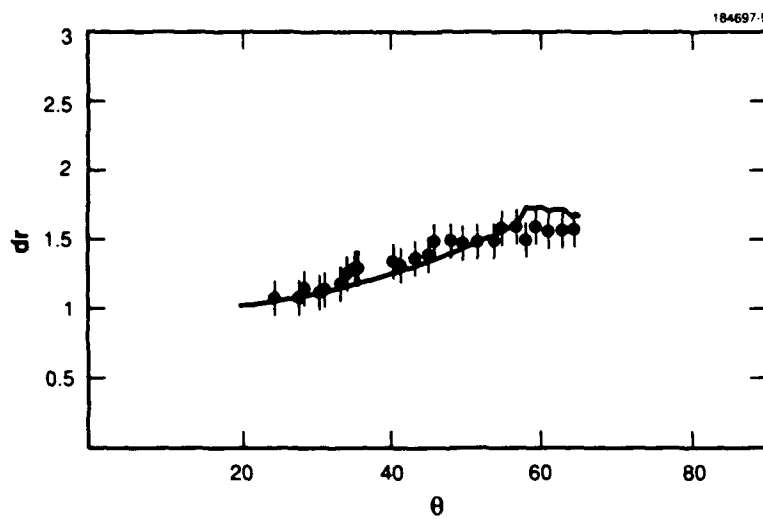


Figure 9. Comparison between the measured extended return length and the corrected calculated return length. The dots are the measurements with one-half resolution-cell error bars.

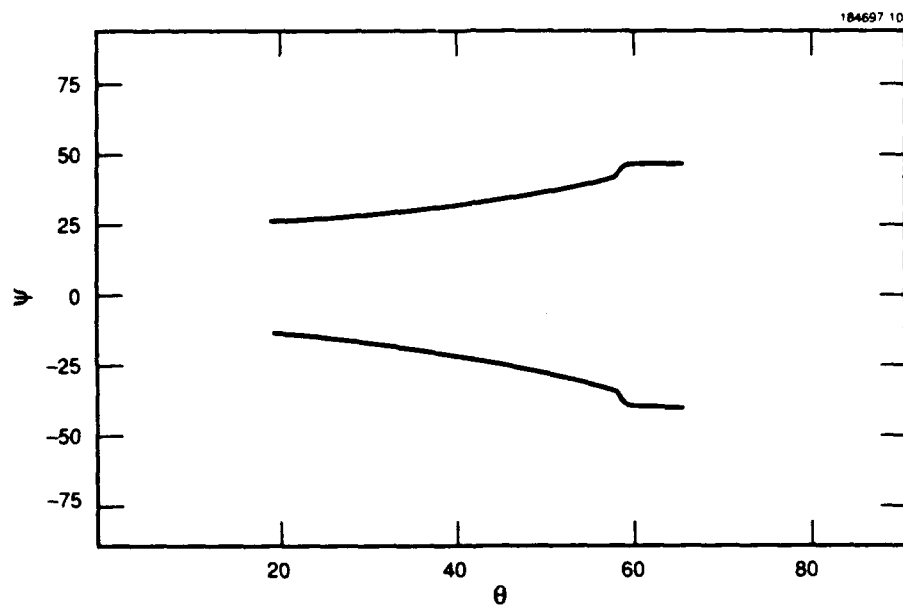


Figure 10. Reflection locations. The upper curve defines the location of the first reflection and the lower curve defines the location of the second reflection.

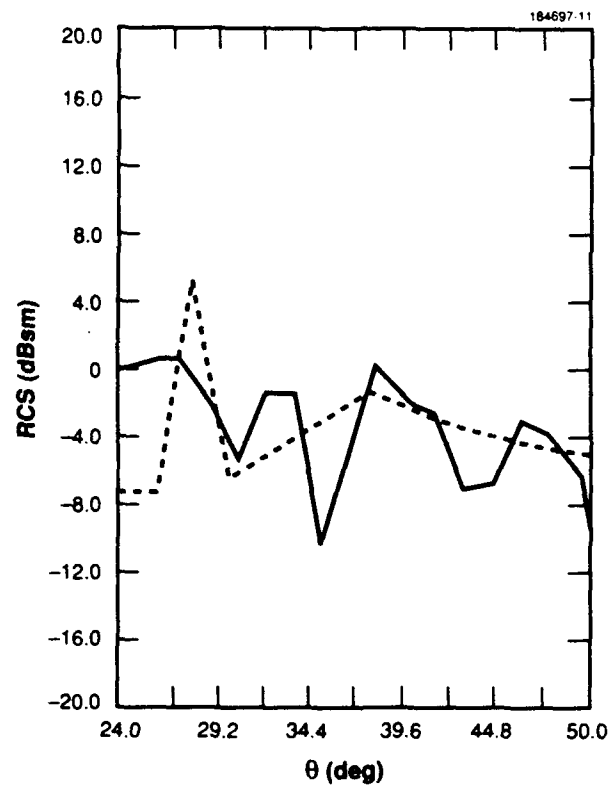


Figure 11. Comparison of the predicted (dashed) and measured radar cross section of the multiple reflection.

#### 4. INVERSE PROBLEM

This section applies the prediction techniques described in Section 3 to the problem of estimating the nozzle parameters from image measurements. In general, this is not a well-posed problem, but by incorporating a suitable number of additional constraints the problem becomes tractable.

In order to take measurements from the images, it is necessary to set up a useful coordinate system. The coordinate system used in this analysis is shown in Figure 12, which also demonstrates the measurements necessary to estimate the shape of the nozzle, i.e.,  $(d, z)$  pairs. This coordinate system is set up such that the measurements do not require knowledge of the shape of the nozzle. For this procedure to produce useful results, a large number of measurements are required (20-30); thus, it is useful to produce overlapped images for the purpose of making the measurements.

Once the measurements have been made, they are used in a optimization loop to calculate the two parameters that describe the nozzle. This loop is depicted in Figure 13. In order for this optimization loop to correctly converge, it is necessary to have a good initial estimate of the nozzle parameters. This estimate is derived from measurements of the diffraction points at the end of the nozzle and the scattering from the outside of the throat of the nozzle.

The optimization technique was used with the measurements from images described in Section 3 to estimate the nozzle parameters. The estimated parameters were found to be

$$\begin{aligned}\hat{A} &= 8.5 \text{ m}, \\ \hat{B} &= 1.2 \text{ m},\end{aligned}\tag{37}$$

where the parameters were bound in the minimization within the intervals  $A \in [7, 10]$  and  $B \in [1, 2]$ . These estimated parameters are within 6 percent of those derived from the engineering drawings. During the minimization process there were many local minimums found around the desired solution. It is therefore imperative that a good initial guess of the parameters be made before the optimization process is initiated; several optimizations must also be performed to guarantee that a global minimum has been found. It is important to understand that several combinations of  $A$  and  $B$  can be used to describe the nozzle to within a prescribed accuracy. Any major defects in the nozzle would clearly show up in these measurements.

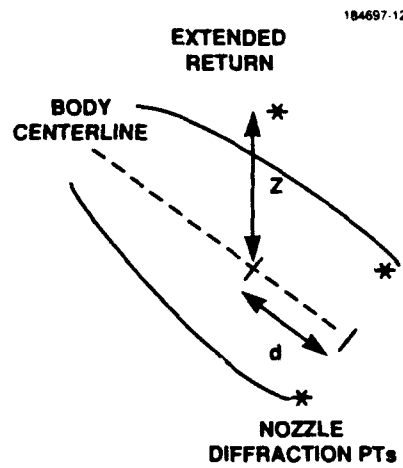


Figure 12. Image-measurement coordinate system.

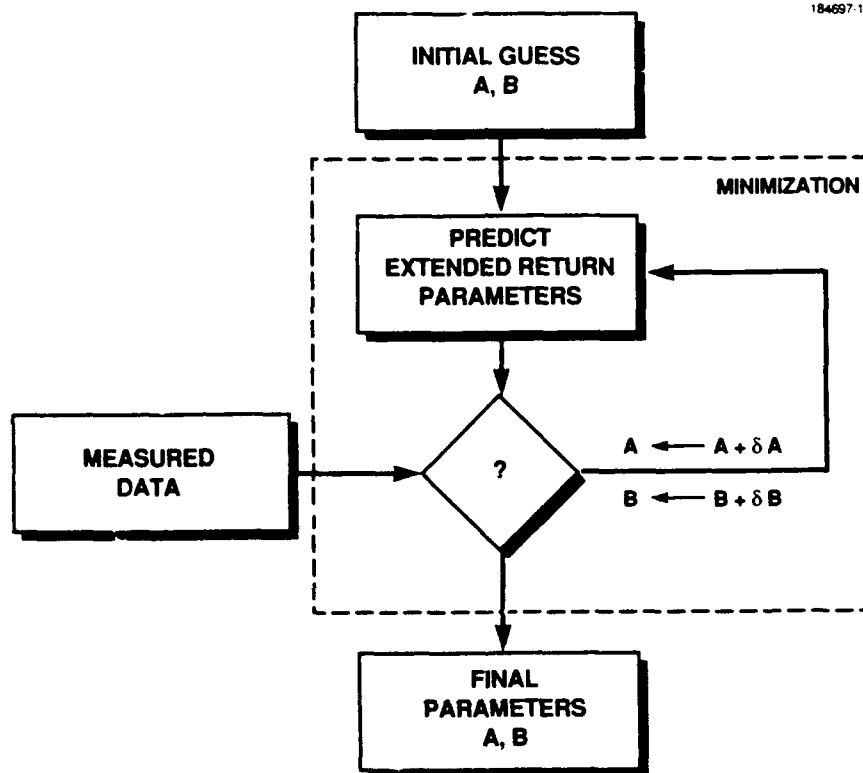


Figure 13. Depiction of the optimization loop.

## 5. SUMMARY

This report examined scattering from a rocket nozzle that could be modeled as a section of an ellipse. This modeling process yielded excellent agreement between measured and predicted ray-path length data from images. Radar cross-section estimates were also calculated for the measured three-reflection ray detected by the radar.

The report concluded by demonstrating how this prediction technique could be used to determine the parameters of a rocket nozzle from direct measurements from a set of images. Through the use of an optimization loop, the parameters were varied until the calculated and measured prediction extended return lengths matched. This process yielded calculated parameters that were within 6 percent of those measured from the engineering drawings.

The Geometric Optics (GO) technique is valid for a wide range of cavity-scattering problems, as long as the cavity is away from resonance and is large compared to the incident field's wavelength. A more general shape description of the cavity/nozzle could have been used, but this report demonstrated the usefulness of the elliptical approximation. If the nozzle had been straight, not curved, the GO method would have failed because there would have been a caustic at the point where the internal surface became specular to the radar. For this case a more elaborate method is needed to calculate the amplitude of the response.

## APPENDIX A SURFACE PARAMETERS FOR A BODY OF REVOLUTION

In this appendix the important surface parameters for an arbitrary body of revolution (BOR) are derived. The geometry used in this appendix is shown in Figure A-1. The analysis starts by writing the parameterization of the surface as

$$\mathbf{X} = f(\theta) \cos \phi \mathbf{u} + f(\theta) \sin \phi \mathbf{v} + g(\theta) \mathbf{w} \quad , \quad (\text{A.1})$$

then forming the two surface tangent vectors

$$\mathbf{X}_\theta = f'(\theta) \cos \phi \mathbf{u} + f'(\theta) \sin \phi \mathbf{v} + g'(\theta) \mathbf{w} \quad , \quad (\text{A.2})$$

$$\mathbf{X}_\phi = -f(\theta) \sin \phi \mathbf{u} + f(\theta) \cos \phi \mathbf{v} + g(\theta) \mathbf{w} \quad . \quad (\text{A.3})$$

The normal can then be formed by forming the cross product  $\mathbf{X}_\theta \times \mathbf{X}_\phi$ ; after normalization, this leads to the expression for the unit normal

$$\mathbf{N} = \frac{1}{\sqrt{(fg')^2 + (ff')^2}} (-fg' \cos \phi \mathbf{u} - fg' \sin \phi \mathbf{v} + ff' \mathbf{w}) \quad . \quad (\text{A.4})$$

In order to describe the surface of the BOR, it is necessary to compute various derivatives of the surface normal. These derivatives are listed below:

$$\mathbf{N}_\theta = \eta [-fg' \cos \phi \mathbf{u} - fg' \sin \phi \mathbf{v} + ff' \mathbf{w}] \quad (\text{A.5})$$

$$+ \zeta [-\cos \phi (fg'' + f'g') \mathbf{u} + -\sin \phi (fg'' + f'g') \mathbf{v} + (f'f' + ff'') \mathbf{w}] \quad (\text{A.6})$$

and

$$\mathbf{N}_\phi = \zeta [fg' \sin \phi \mathbf{u} + -fg' \cos \phi \mathbf{v}] \quad , \quad (\text{A.7})$$

where

$$\eta = -\frac{(fg')[fg'' + f'g'] + 2(ff')[f'f' + ff'']}{((fg')^2 + (ff')^2)^{1.5}} \quad (\text{A.8})$$

and

$$\zeta = \frac{1}{\sqrt{(fg')^2 + (ff')^2}} \quad . \quad (\text{A.9})$$

The surface of the BOR can be described in either the First Fundamental Form,

$$I = d\mathbf{X} \cdot d\mathbf{X} = Ed\theta^2 + 2Fd\theta d\phi + Gd\phi^2 \quad , \quad (\text{A.10})$$

where

$$E = \mathbf{X}_\theta \cdot \mathbf{X}_\theta = f'^2 + g'^2 \quad (\text{A.11})$$

$$F = \mathbf{X}_\theta \cdot \mathbf{X}_\phi = 0 \quad (\text{A.12})$$

$$G = \mathbf{X}_\phi \cdot \mathbf{X}_\phi = f^2 \quad , \quad (\text{A.13})$$

or in the Second Fundamental Form,

$$II = -d\mathbf{X} \cdot d\mathbf{N} = Ld\theta^2 + 2Md\theta d\phi + Nd\phi^2 \quad , \quad (\text{A.14})$$

where

$$L = -\mathbf{X}_\theta \cdot \mathbf{N}_\theta = -\zeta(g'ff'' - f'fg'') \quad (\text{A.15})$$

$$M = -\frac{1}{2}(\mathbf{X}_\theta \cdot \mathbf{N}_\phi + \mathbf{X}_\phi \cdot \mathbf{N}_\theta) = 0 \quad (\text{A.16})$$

$$N = -\mathbf{X}_\phi \cdot \mathbf{N}_\phi = \zeta f^2 g' \quad . \quad (\text{A.17})$$

The principle curvatures,  $\kappa_{1,2}$ , are found by solving the quadratic

$$(EG - F^2)\kappa^2 - (EN + GL - 2FM)\kappa + (LN - M^2) = 0 \quad . \quad (\text{A.18})$$

The quadratic equation can be solved; this yields

$$\kappa_1 = \frac{g'}{f} \frac{1}{\sqrt{f'^2 + g'^2}} \quad (\text{A.19})$$

and

$$\kappa_2 = \frac{f'g'' - g'f''}{(f'^2 + g'^2)^{\frac{3}{2}}} \quad . \quad (\text{A.20})$$

It can be shown that if  $M = F = 0$ , the principle directions of curvature are given by

$$\mathbf{e}_1 = \frac{\mathbf{X}_\theta}{|\mathbf{X}_\theta|} \quad (\text{A.21})$$

and

$$\mathbf{e}_2 = \frac{\mathbf{X}_\phi}{|\mathbf{X}_\phi|} \quad (\text{A.22})$$

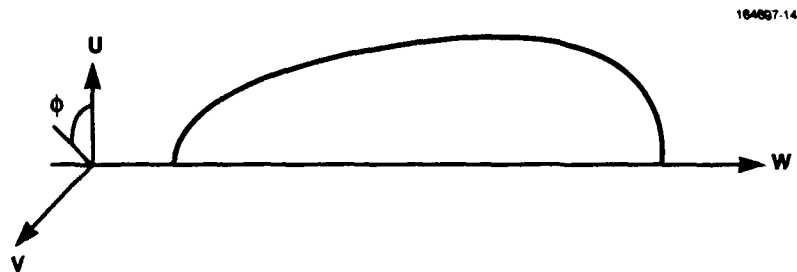


Figure A-1. Body-of-revolution coordinate system.

## APPENDIX B SURFACE PARAMETERS FOR THE NOZZLE

For the case of an elliptic generating arc with

$$f(\theta) = B \sin \theta \quad (B.1)$$

and

$$g(\theta) = A \cos \theta \quad , \quad (B.2)$$

the surface parameters are found to be the following:

$$E = B^2 \cos^2 \theta + A^2 \sin^2 \theta \quad (B.3)$$

$$F = 0 \quad (B.4)$$

$$G = B^2 \sin^2 \theta \quad (B.5)$$

$$L = \frac{-AB}{\sqrt{A^2 \sin^2 \theta + B^2 \cos^2 \theta}} \quad (B.6)$$

$$M = 0 \quad (B.7)$$

$$N = \frac{AB \sin^2 \theta}{\sqrt{A^2 \sin^2 \theta + B^2 \cos^2 \theta}} \quad (B.8)$$

Using the results of Appendix A, the principle curvatures are found to be

$$\kappa_1 = \frac{-AB}{(A^2 \sin^2 \theta + B^2 \cos^2 \theta)^{3/2}} \quad (B.9)$$

and

$$\kappa_2 = \frac{-\frac{A}{B}}{(A^2 \sin^2 \theta + B^2 \cos^2 \theta)^{1/2}} \quad (B.10)$$

## REFERENCES

1. D. Ausherman, A. Kozma, J. Walker, H. Jones, and E. Poggio, "Developments in radar imaging," *IEEE Transactions on Aerospace and Electronic Systems* AES-20, 363-400 (1984).
2. G. James, *Geometrical Theory of Diffraction for Electromagnetic Waves*, London: Peter Peregrinus Ltd., 3 ed. (1986).
3. C.A. Balanis, *Advanced Engineering Electromagnetics*, New York: John Wiley and Sons (1989).

REPORT DOCUMENTATION PAGE			Form Approved OMB No. 0704-0188	
<small>Public reporting burden for this collection of information is estimated to average 1 hour per response, including the time for reviewing instructions, searching existing data sources, gathering and maintaining the data needed and completing and reviewing the collection of information. Send comments regarding this burden estimate or any other aspect of this collection of information, including suggestions for reducing this burden to: Washington Headquarters Services, Directorate for Information Operations and Reports, 1215 Jefferson Davis Highway, Suite 1204, Arlington, VA 22202-4302, and to the Office of Management and Budget, Paperwork Reduction Project (0704-0188), Washington, DC 20503.</small>				
1. AGENCY USE ONLY (Leave blank)	2. REPORT DATE 3 January 1992	3. REPORT TYPE AND DATES COVERED Technical Report		
4. TITLE AND SUBTITLE Scattering Measurements and Predictions for a Delta Stage II Rocket Nozzle		5. FUNDING NUMBERS  C — F19628-90-0002 PE — 12424F, 31310F, 63223C, 63220C PR — 80		
6. AUTHOR(S)  Thomas G. Moore				
7. PERFORMING ORGANIZATION NAME(S) AND ADDRESS(ES)  Lincoln Laboratory, MIT P.O. Box 73 Lexington, MA 02173-9108		8. PERFORMING ORGANIZATION REPORT NUMBER  TR-934		
9. SPONSORING/MONITORING AGENCY NAME(S) AND ADDRESS(ES)  FTD/SQDRA                      AFSPACCOM Wright Patterson AFB        Peterson AFB Ohio 45433                      Colorado 80914		10. SPONSORING/MONITORING AGENCY REPORT NUMBER  ESD-TR-91-161		
11. SUPPLEMENTARY NOTES  None				
12a. DISTRIBUTION/AVAILABILITY STATEMENT  Approved for public release; distribution is unlimited.		12b. DISTRIBUTION CODE		
13. ABSTRACT (Maximum 200 words)  This report develops the theory necessary to analyze radar images of non-conical rocket nozzle sections. The theory is based on Geometric Optics and ray tracing. The location of the expected response in an inverse synthetic-aperture radar image of this type of rocket nozzle is developed. The ability to predict the location of the response is used to develop a technique for reconstructing the shape of a rocket nozzle from measurements made from an image. The theory is applied to a pass of data collected on a tumbling Delta Stage II rocket body. The data were collected by a millimeter-wave radar with a center frequency of 35 GHz and a bandwidth of 1 GHz. The theoretical predictions of the scattered fields are first validated using these data and drawings of the rocket nozzle. The inverse method is then applied to the data to determine the shape of the nozzle. The agreement between the nozzle shape predicted by the inverse method and drawings of the nozzle agree to within 6 percent.				
14. SUBJECT TERMS			15. NUMBER OF PAGES 42	
			16. PRICE CODE	
17. SECURITY CLASSIFICATION OF REPORT Unclassified	18. SECURITY CLASSIFICATION OF THIS PAGE Unclassified	19. SECURITY CLASSIFICATION OF ABSTRACT Unclassified	20. LIMITATION OF ABSTRACT SAR	